Available online at www.sciencedirect.com

SciVerse ScienceDirect

Acta Materialia 59 (2011) 7615–7626

Acta MATERIALIA

www.elsevier.com/locate/actamat

Effects of Yb and Zr microalloying additions on the microstructure and mechanical properties of dilute Al–Sc alloys

Marsha E. van Dalen [a,*], Thomas Gyger [a], David C. Dunand [a], David N. Seidman [a,b]

[a] Northwestern University, Department of Materials Science & Engineering, Evanston, IL 60208, USA
[b] Northwestern University Center for Atom-Probe Tomography (NUCAPT), Evanston, IL 60208, USA

Received 13 February 2011; received in revised form 8 September 2011; accepted 9 September 2011
Available online 15 October 2011

Abstract

It is known that Zr and Yb partition to the Al_3Sc precipitates created during aging when microalloyed separately in dilute binary Al–Sc alloys. Addition of Zr delays precipitate coarsening, thereby improving the coarsening resistance of the ternary Al-Sc-Zr alloys. Addition of Yb increases the resistance against dislocation climb, thereby improving the creep resistances of the ternary Al-Sc-Yb alloys. A combination of microhardness, creep, and atom probe tomography measurements provide evidence that these effects of Zr and Yb additions are cumulative in quaternary dilute Al–Sc–Yb–Zr alloys: Yb increases their creep resistance at 300 °C compared with ternary Al–Sc–Zr alloys and Zr improves their coarsening resistance at 300 °C compared with ternary Al–Sc–Yb alloys. Additionally, excellent coarsening resistance is observed at 350 and 375 °C.

Keywords: Aluminum alloys; Nucleation; Precipitation; Coarsening; Creep

1. Introduction

Small additions of scandium to aluminum (below the maximum solubility limit of 0.23 at.% Sc at the eutectic temperature) result, upon aging, in the formation of nanoscale coherent Al_3Sc precipitates with $L1_2$ structure, which remain coarsening resistant up to ~300 °C [1–8]. When cast to produce coarse, millimeter diameter grains and aged to form nanoscale Al_3Sc precipitates, binary Al–Sc alloys exhibit good creep resistance as a result of precipitation strengthening up to ~300 °C, above which rapid coarsening of the Al_3Sc precipitates occurs [9,10]. Increasing the coarsening resistance of the precipitates with additional alloying elements results in improved long-term creep resistance for this alloy and/or higher creep temperatures.

Microalloying binary Al–Sc alloys with elements with small diffusivities in Al (in particular Ti [11], Zr [12] and/or Hf [13]) leads to slower coarsening kinetics of the Al_3Sc precipitates. In the extensively studied Al–Sc–Zr system, Zr partitions to the Al_3Sc precipitates forming coarsening-resistant $Al_3(Sc_{1-x}Zr_x)$ precipitates [12,14,15], which retain their $L1_2$ structure. While up to half of the Sc atoms can be replaced by Zr atoms [16,17], the Zr concentrations in the precipitates of Al–Sc–Zr alloys are, however, smaller than this maximum value, $x = 0.5$ [12,18–20], as a result of the small diffusivity of Zr in Al [21]. Several experimental studies have demonstrated that Zr segregates at the α-Al/Al_3Sc heterophase interface, forming a Zr-enriched $Al_3(Sc_{1-x}Zr_x)$ outer shell [13–15,18,22–24]. Furthermore, lattice kinetic Monte Carlo simulations indicate that the formation of this shell is due to the large disparity in diffusivities between Sc and Zr [25].

Rare earth (RE) elements are attractive ternary additions to Al–Sc alloys for many reasons. First, many RE elements substitute for Sc in $Al_3Sc(L1_2)$ precipitates forming $Al_3(Sc_{1-x}RE_x)$ $(L1_2)$ with high RE solubility, thereby replac-

* Corresponding author. Present address: Momentive Performance Materials, 24400 Highland Road, Richmond Heights, OH 44143, USA. Tel.: +1 440 953 7397.
E-mail address: marsha.vandalen@gmail.com (M.E. van Dalen).

1359-6454/$36.00 © 2011 Acta Materialia Inc. Published by Elsevier Ltd. All rights reserved.
doi:10.1016/j.actamat.2011.09.019

ing the more expensive Sc [26–28]. Secondly, RE elements have diffusivities in Al [29,30] that are significantly greater than those of Zr or Ti [31], so that RE atoms are incorporated into $Al_3Sc(L1_2)$ precipitates more rapidly than Zr or Ti atoms. Thirdly, unlike Ti or Zr [17], RE elements increase the lattice parameter mismatch between α-Al(fcc) and $Al_3(Sc_{1-x}RE_x)$ $(L1_2)$ [26,27], which can increase the creep resistance of an alloy by increasing dislocation–precipitate elastic interactions [32]. Specifically, replacing some of the Sc with Yb or Gd [33,34] and Y, Dy or Er [35] results in improved creep resistance. Neither peak microhardness nor coarsening resistance are, however, affected [36,37].

Herein we report on the microstructural temporal evolution and creep properties of binary Al–Sc alloys microalloyed with both Yb (used to improve creep resistance) and Zr (added to enhance coarsening resistance). The interactions among the alloying elements and the resulting mechanical properties are reported and discussed.

2. Experimental procedures

Two microalloying compositions were chosen to maximize the probability that the alloys were in the single α-Al(fcc) phase field during homogenization, permitting complete homogenization. Each alloy was produced by diluting small quantities of Al–1.2 at.% Sc (Ashurst), Al–0.17 at.% Yb (Stanford Materials), and Al–2.96 at.% Zr (Alcoa) master alloys in 99.99% pure Al. The compositions of the alloys are Al–0.07Sc–0.02Yb–0.004Zr and Al–0.06Sc–0.02Yb–0.02Zr (at.%), with impurity concentrations of 22 ± 3 at. p.p.m. iron and 38 ± 5 at. p.p.m. silicon, as verified by direct coupled plasma mass spectroscopy performed by Wah Chang (Albany, OR). Hereafter all concentrations are expressed as atomic percentages (at.%) or atomic parts per million (at. p.p.m.) and these alloys are referred to as the low Zr and high Zr alloys. They were melted in an alumina crucible in a resistively heated furnace at 750 °C in air. After thorough stirring, the melt was cast into a graphite mold resting on a large copper platen. Homogenization was performed at 640 °C for 72 h in air and terminated by water quenching to room temperature. Aging was performed in air at 300, 350 or 375 °C and terminated by water quenching.

Vickers microhardness measurements were performed at room temperature using a 200 g load for 10 s on aged samples, which were mounted in acrylic and ground to a 1 μm surface finish. Ten measurements were performed on each sample. Compression creep tests were performed in air on specimens, 8 mm diameter and 16 mm length aged for 96 h at 300 °C, using a nickel-based superalloy compression cage lubricated with a boron nitride coating to minimize friction between the cage and the sample. The displacement was measured with a linear variable differential transducer connected to an extensometer. Prior to testing the creep samples were soaked at the testing temperature for 2 h to ensure a uniform temperature. During testing sufficient time was allowed to reach a minimum strain rate for each successively higher load applied to the sample. The creep experiments were terminated when a sample achieved an engineering strain of 10%. No sample was crept for more than 10 days to ensure that the precipitates did not coarsen significantly during the test.

Sample blanks for local electrode atom probe (LEAP) tomography were produced by mechanically grinding the material to a square cross-section of $\sim 300 \times 300\ \mu m^2$. An atomically sharp microtip was then created by electropolishing: initial polishing was performed with a solution of 10 vol.% perchloric acid in acetic acid, while final polishing was performed with a solution of 2 vol.% perchloric acid in butoxyethanol. LEAP tomography was performed at a specimen temperature of 30 K using a LEAP 3000 (Cameca, (formerly Imago Scientific Instruments) Madison, WI) [38] operated in voltage pulsing mode at a pulse repetition rate of 200 kHz and a 20% pulse fraction (ratio of pulse voltage to the steady-state dc voltage). Proximity histogram plots (proxigrams for short) [39] were calculated employing the APEX [40] or IVAS (Cameca) software programs, using an isoconcentration surface of 9 at.% Sc, corresponding to the inflection point in the Sc concentration profile. The average precipitate composition was determined by counting the number of atoms in the precipitates using a cluster search algorithm (IVAS).

3. Results

3.1. Microhardness evolution upon aging at 300 °C

The Vickers microhardness exhibits a significantly longer incubation time upon aging at 300 °C for both quaternary Al–Sc–Yb–Zr alloys (Fig. 1), compared with a

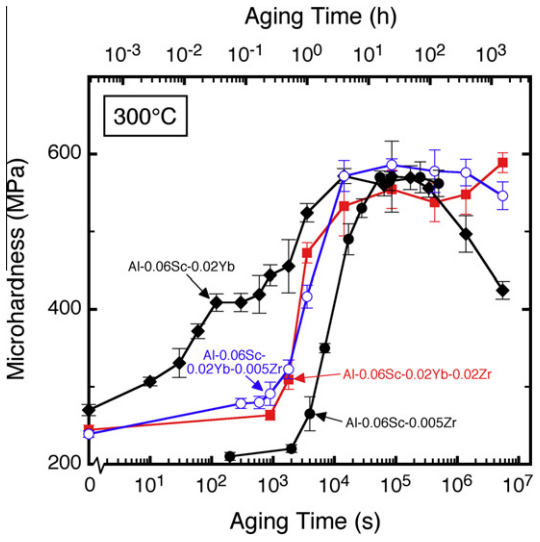

Fig. 1. Vickers microhardness versus aging time at 300 °C for the two quaternary Al–Sc–Yb–Zr alloys with low Zr and high Zr concentrations. Also plotted for comparison are the aging responses of ternary alloys without Zr (Al–0.06Sc–0.02Yb [34,36]) and without Yb (Al–0.06Sc–0.005Zr [52]).

ternary Al–0.06Sc–0.02Yb alloy containing no Zr (hereafter referred to as Al–Sc–Yb) studied earlier [36]. The low Zr quaternary alloy required a shorter incubation time compared with the high Zr alloy (<5 min versus ~15 min). For the latter alloy the microhardness increased by only 20 MPa after 15 min aging, while for the low Zr alloy the microhardness increased by 40 MPa after aging for 5 min. Both quaternary Al–Sc–Yb–Zr alloys required an incubation time shorter than a ternary Al–0.06Sc–0.005Zr alloy without Yb (Fig. 1, from data reported in van Dalen et al. [34]), which only exhibited significant hardening after aging for 30–60 min.

For both Al–Sc–Yb–Zr alloys there was only one rapid increase in microhardness, between 15 and 60 min. In contrast, the Al–Sc–Yb alloy exhibited a distinct plateau in microhardness between the first and second rapid increases in microhardness, which is attributed to the initial precipitation of Yb-rich $Al_3(Yb_{1-x}Sc_x)$ precipitates, followed by a second precipitation stage of Sc-rich $Al_3(Sc_{1-x}Yb_x)$ precipitates, as Sc diffuses into the Yb-rich precipitates [34]. Additionally, both Al–Sc–Yb–Zr alloys retained their microhardness values for up to 64 days of aging at 300 °C, unlike the ternary Al–Sc–Yb alloy, which begins to lose its microhardness after 96 h.

3.2. Microstructure evolution upon aging at 300 °C

In the homogenized unaged state there were no precipitates visible in the three-dimensional (3-D) LEAP tomographic reconstruction for either of the Al–Sc–Yb–Zr alloys. After 15 min aging there was, however, evidence that precipitation was occurring in both Al–Sc–Yb–Zr alloys, as demonstrated in Fig. 2 for the low Zr alloy, which exhibited precipitates with an average radius $\langle R\rangle$ of 0.67 ± 0.19 nm. The largest precipitate in the dataset has a maximum value R_{max} of 1.32 nm. The high Zr alloy contained smaller precipitates: after 15 min $\langle R\rangle = 0.56 \pm 0.08$ nm and $R_{max} = 0.82$ nm. These quantities were determined using the envelope method [41,42]. The precipitate size distributions for the Zr-containing alloys, including sub-critical precipitates, are displayed in Fig. 3.

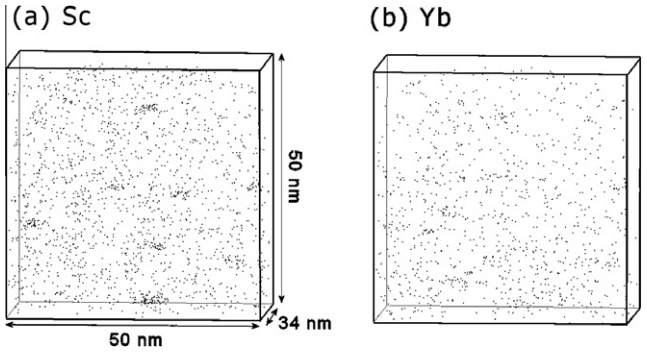

Fig. 2. Three-dimensional reconstruction of a LEAP tomographic data set (2.6 million atoms) for the low Zr alloy after 15 min aging at 300 °C showing precipitates with average radius $\langle R\rangle = 0.67 \pm 0.19$ nm: (a) Sc atoms; (b) Yb atoms.

The Yb/(Yb + Sc) ratio of atomic concentrations in the precipitates ($C^{\alpha'}_{Yb}(R)/(C^{\alpha'}_{Yb}(R) + C^{\alpha'}_{Sc}(R))$), where α' refers to the $L1_2$ structure precipitate phase, is displayed after 15 min aging in Fig. 4a and b. There is a wide range of values of $C^{\alpha'}_{Yb}(R)/(C^{\alpha'}_{Yb}(R) + C^{\alpha'}_{Sc}(R))$ for individual precipitates. The average value for the ratio is 0.37 ± 0.26 for the low Zr alloy and 0.46 ± 0.23 for the high Zr alloy. These values are greater than $C^{\alpha'}_{Yb}(R)/(C^{\alpha'}_{Yb}(R) + C^{\alpha'}_{Sc}(R))$ based on the overall alloy compositions, which are 0.22 and 0.25, respectively. For comparison, $C^{\alpha'}_{Yb}(R)/(C^{\alpha'}_{Yb}(R) + C^{\alpha'}_{Sc}(R))$ is displayed for the ternary Al–Sc–Yb alloy (Fig. 4c), which has a larger ratio of 0.56 ± 0.25 than either of the two Zr-containing quaternary alloys [33]. Furthermore, the Al–Sc–Yb alloy also has a higher maximum precipitate radius R_{max} of 2.6 nm.

After 1 h aging the average precipitate radius has increased to $\langle R\rangle = 0.81 \pm 0.38$ nm for the low Zr alloy and $\langle R\rangle = 0.92 \pm 0.61$ nm for the high Zr alloy. Fig. 5a and b exhibits a clear trend of decreasing values of $C^{\alpha'}_{Yb}(R)/(C^{\alpha'}_{Yb}(R) + C^{\alpha'}_{Sc}(R))$ with increasing values of $\langle R\rangle$. For precipitates with $R < 0.75$ nm most of the precipitates have values of $C^{\alpha'}_{Yb}(R)/(C^{\alpha'}_{Yb}(R) + C^{\alpha'}_{Sc}(R))$ greater than for the overall alloy composition, although there is significant scatter. In contrast, precipitates with $R > 1$ nm always exhibit a smaller value of $C^{\alpha'}_{Yb}(R)/(C^{\alpha'}_{Yb}(R) + C^{\alpha'}_{Sc}(R))$ than the overall alloy ratio. Fig. 6 shows the fraction of solute (Yb + Sc) that has precipitated after 15 min and 1 h aging. Slower precipitation kinetics are observed with Zr-containing alloys: after 1 h the fraction of the total (Yb + Sc) solute precipitated is significantly smaller for the Zr-containing alloys than for the Zr-free Al–Sc–Yb alloy (~50% vs. 70%) (Fig. 6).

Fig. 7 shows the proxigram for the high Zr alloy after the longest aging time (1536 h or 64 day), where the concentrations of Sc, Yb and Zr are plotted as a function of distance from the α-Al/$Al_3(Yb_{1-x-y}Sc_xZr_y)$ interface. While there is a nearly uniform distribution of Yb and Sc in the precipitates, Zr is segregated at the α-Al/$Al_3(Yb_{1-x-y}Sc_xZr_y)$ heterophase interface. The concentration of Sc + Yb + Zr sums to >25% due, most probably, to field evaporation differences between the elements [43–45].

3.3. Partial radial distribution functions after aging at 300 °C

The partial radial distribution functions (RDF) [46,47] for interactions among each of the elements were measured to shed light on the mechanism causing the increased incubation time required for precipitation in the presence of Zr (Fig. 1). The standard definition of a RDF [48] at a given radial distance is defined as the average concentration of component i around a given solute species X, when summed over all of the atoms of type X, by:

$$\mathrm{RDF} = \frac{\langle C_i^X(r)\rangle}{C_i^o} = \frac{1}{C_i^o}\sum_{k=1}^{N_X}\frac{N_i^k(r)}{N_{tot}^k(r)} \quad (1)$$

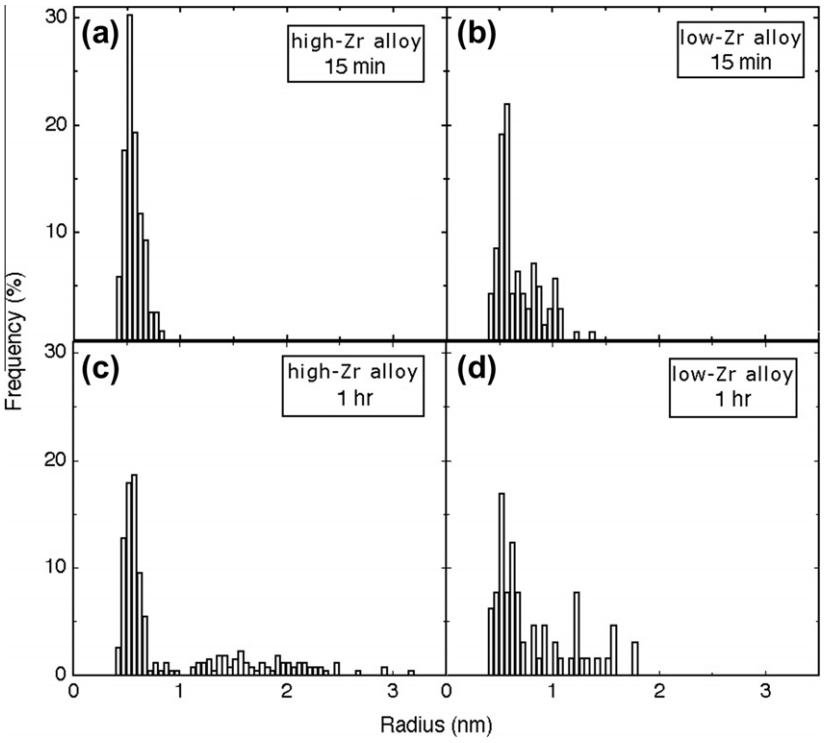

Fig. 3. Precipitate size distributions (PSD) for aging at 300 °C: (a) high Zr alloy, 15 min (119 precipitates); (b) low Zr alloy, 15 min (138 precipitates); (c) high Zr alloy, 1 h (273 precipitates); (d) low Zr alloy, 1 h (65 precipitates).

where C_i^o is the overall concentration of element i in the alloy, $C_i^X(r)$ is the concentration of component i at a distance r from component X, $N_{tot}^k(r)$ is the total number of atoms in the shell at a distance r from the kth atom of type X, and $N_i^k(r)$ is the number of atoms of type i in the shell at a distance r from the kth atom of type X. An advantage of performing a partial RDF analysis using 3-D LEAP tomography is that the analysis is performed in direct space, whereas (X-ray or neutron) scattering experiments are performed in reciprocal space, so the results need to be deconvoluted. Only the partial RDF data for $r \geqslant 0.2$ nm are presented as the physical interpretation at smaller r is difficult due to possible ion trajectory effects [49,50]. RDF values of unity describe perfectly random distributions, while values that differ from unity describe clustering or ordering. The absolute magnitude of these processes can be compared with the partial RDF amplitude ($A = [\text{partial RDF}(r) - 1]$), where $A > 0$ indicates a greater concentration than the overall concentration (positive correlation) and $A < 0$ implies a smaller one (negative correlation).

Partial RDF are presented in Figs. 8–10, and were determined employing all solute atoms in the dataset of the two quaternary alloys. No precipitates are visible in the as-quenched state in either alloy, thus all of the solute atoms are in the α-Al matrix. A partial RDF for the high Zr alloy after 15 min aging is presented for comparison. There are some precipitates visible after 15 min in this alloy, so the partial RDF is a convolution of the atoms in the α-Al matrix as well as atoms in the precipitates. A partial RDF at this aging time will still display the effect of atomic interactions, compared with the as-quenched state. A study of Ni–Cr–Al alloys [46], performed for longer aging times (>64 h), obtained values systematically greater than unity, rather than oscillations about unity. This was attributed to precipitation at the longer aging times.

For the high Zr alloy values greater than unity are observed for the partial Yb–Zr and Zr–Yb RDF for distances <1 nm, both in the as-quenched state and after 15 min of aging (Fig. 8a). After 15 min of aging the maximum value, which is at the first nearest neighbor (NN) distance, is 1.75 (i.e. 1.75 times the average concentration in the alloy). In the low Zr alloy in the as-quenched state there are peaks between the second and third NN distances (Fig. 9a). The interaction between Yb and Zr is, however, less obvious than in the high Zr alloy (Fig. 8a).

The partial Yb–Yb RDF demonstrates that in the as-quenched state the high Zr alloy has values greater than unity (Fig. 10b), indicating that some clustering has occurred. After 15 min aging Yb is involved in forming $Al_3(Yb_{1-x}Sc_x)$ precipitates, which is reflected in values exceeding 10 for the partial RDF (Fig. 10b). There are also large values for the Yb–Yb partial RDF of the low Zr alloy in the unaged state (Fig. 10a), with a peak value of 17, indicative of a strong interaction among the Yb atoms in the unaged state.

The Zr–Zr partial RDF for the high Zr alloy in the unaged state has values that remain close to unity, ranging from 0.9 to 1.4 (Fig. 8b). There is no significant change after aging for 15 min, with the maximum value being 1.7. The probable reason for this lack of measurable clustering of Zr atoms is its very small diffusivity in Al [21].

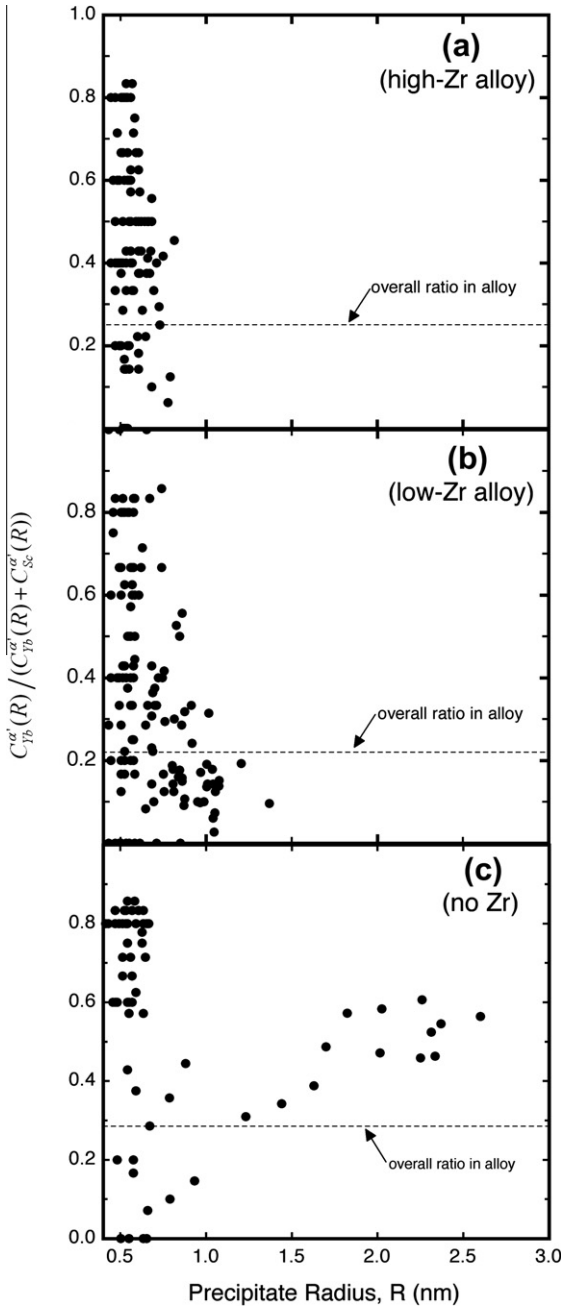

Fig. 4. The atomic concentration ratio $C^{\alpha'}_{Yb}(R)/(C^{\alpha'}_{Yb}(R)+C^{\alpha'}_{Sc}(R))$ versus the precipitate radius R for individual precipitates after aging for 15 min at 300 °C: (a) high Zr quaternary alloy; (b) low Zr quaternary alloy; (c) Zr-free Al–0.06Sc–0.02Yb ternary alloy [34].

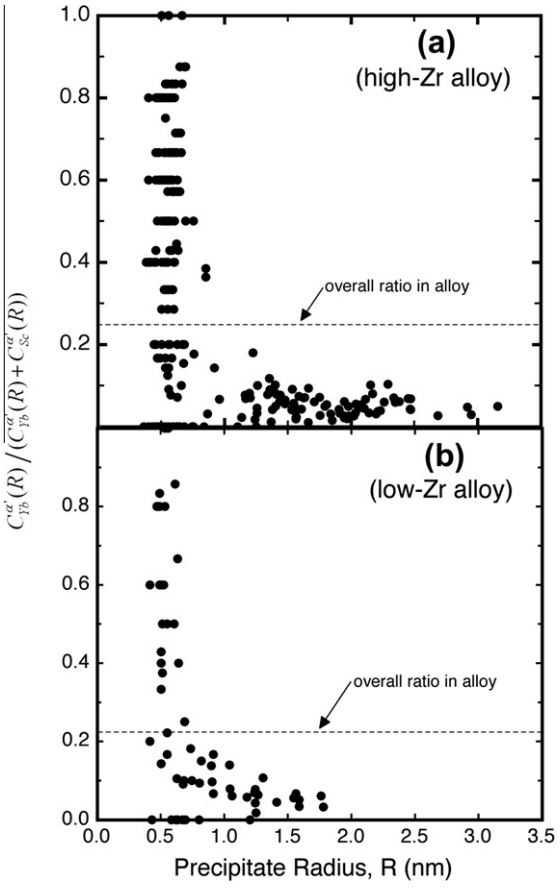

Fig. 5. The atomic concentration ratio $C^{\alpha'}_{Yb}(R)/(C^{\alpha'}_{Yb}(R)+C^{\alpha'}_{Sc}(R))$ versus the precipitate radius R for individual precipitates after aging for 1 h at 300 °C: (a) high Zr alloy; (b) low Zr alloy.

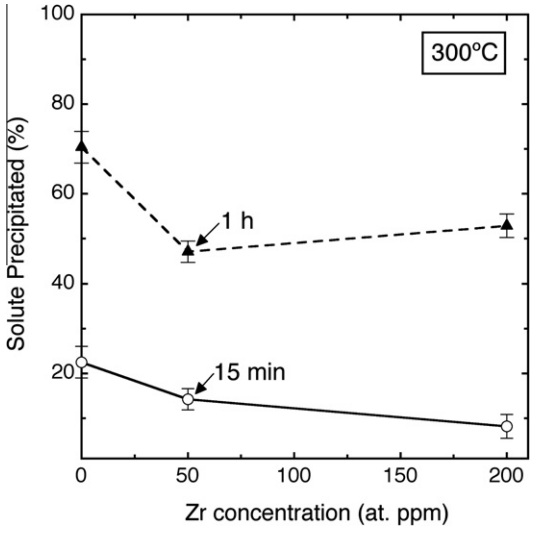

Fig. 6. Percentage of solute (Yb + Sc) precipitated after 15 min and 1 h aging at 300 °C as a function of Zr concentration. The data for Zr-free Al–0.06Sc–0.02Yb are from van Dalen et al. [34].

The low Zr alloy exhibits similar results for the unaged state (Fig. 9b). The range of partial RDF values fluctuates more strongly than for the high Zr alloy because there are fewer Zr atoms, and the partial RDF is a measure of the ratio of the number of atoms. The errors and the significance of the peaks in partial RDF were discussed in van Dalen [33].

In the unaged state of the high Zr alloy there is an attractive interaction between Sc and Yb atoms, but no clear indication of interactions between Sc and Zr atoms (Fig. 8c). While the Sc–Sc partial RDF does not increase much above unity (Fig. 8c), there is a strong repulsive

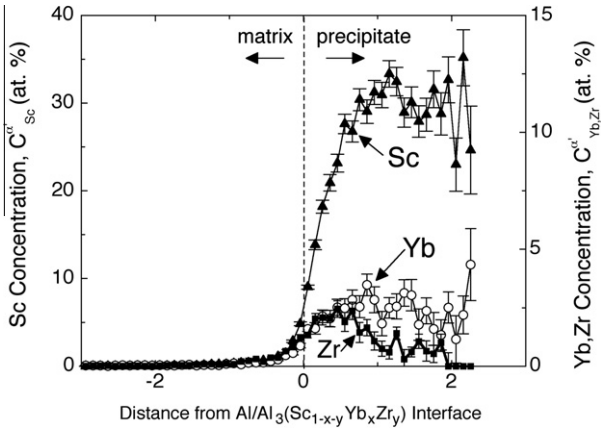

Fig. 7. Proxigram of high Zr alloy after aging for 1536 h at 300 °C, displaying the Sc, Yb and Zr concentrations in the α-Al matrix and precipitates as a function of distance from the matrix/precipitate interface, defined as the a 9 at.% Sc isoconcentration surface.

interaction at the first NN distance and an attractive interaction at the second NN distance, possibly indicating short-range order. For comparison, after 15 min aging there are very clear Sc–Sc and Sc–Yb interactions (Fig. 8d), with the maximum values of the partial RDF peaks being 2.7 and 4, respectively. This is anticipated from the presence of the $Al_3(Yb_{1-x}Sc_x)$ and $Al_3(Sc_{1-x}Yb_x)$ precipitates. The Sc–Zr partial RDF after aging for 15 min remains, however, close to unity. Again, these results for the samples measured after aging represent a convolution of atoms in the precipitates and the α-Al matrix and, hence, are more difficult to interpret compared with the case where no precipitates are present.

Finally, the low Zr alloy in the unaged state exhibits the same repulsive interaction between Sc atoms in the Sc–Sc partial RDF (Fig. 9c). Similarly to the high Zr alloy, little interaction is observed between the Zr and Sc atoms in the unaged state. There is, however, considerable interaction between the Sc and Yb atoms, with partial RDF peaks exceeding 3.

3.4. Coarsening resistance at 300, 350 and 375 °C

The average precipitate radius $\langle R\rangle$ and number density N_v are plotted in Figs. 11 and 12 for both alloys up to an aging time of 1536 h (64 days) at 300 °C. Within experimental error $\langle R\rangle$ and N_v have equal values for the two alloys. The quasi-stationary coarsening behavior of ternary alloys is described by [51]:

$$\langle R(t)\rangle^3 - \langle R(t_o)\rangle^3 = K_{KV}(t - t_o) \quad (2)$$

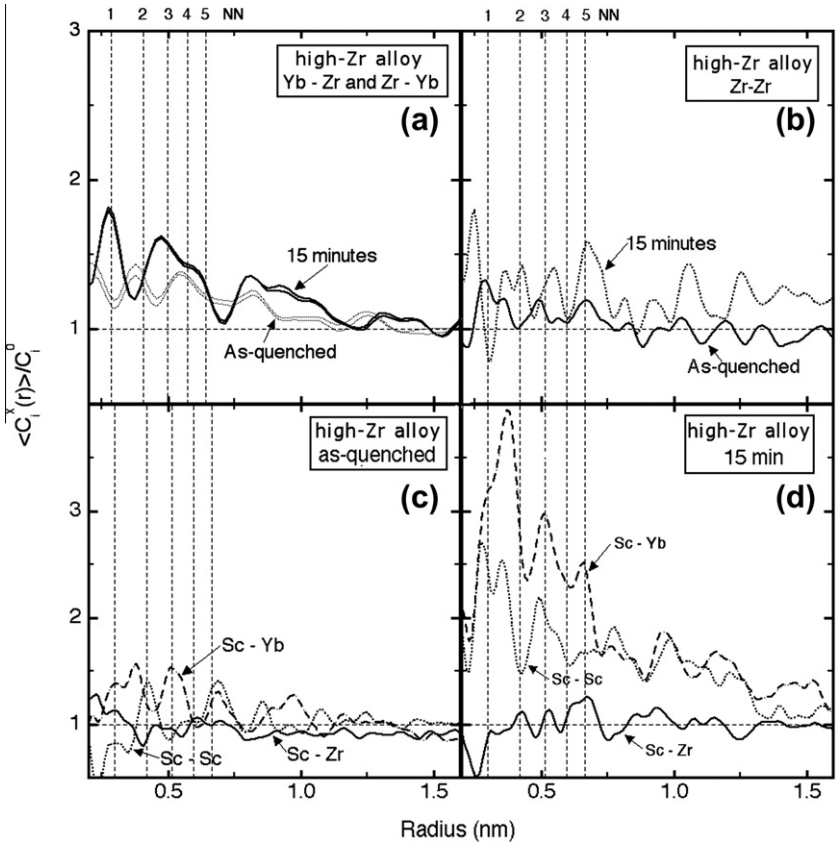

Fig. 8. Partial radial distribution functions (RDF) for the high Zr alloy: (a) Yb–Zr and Zr–Yb in the as-quenched state and after 15 min aging; (b) Zr–Zr in the as-quenched state and after 15 min aging at 300 °C; (c) Sc–Yb, Sc–Sc and Sc–Zr in the quenched state; (d) Sc–Yb, Sc–Sc and Sc–Zr after 15 min aging at 300 °C.

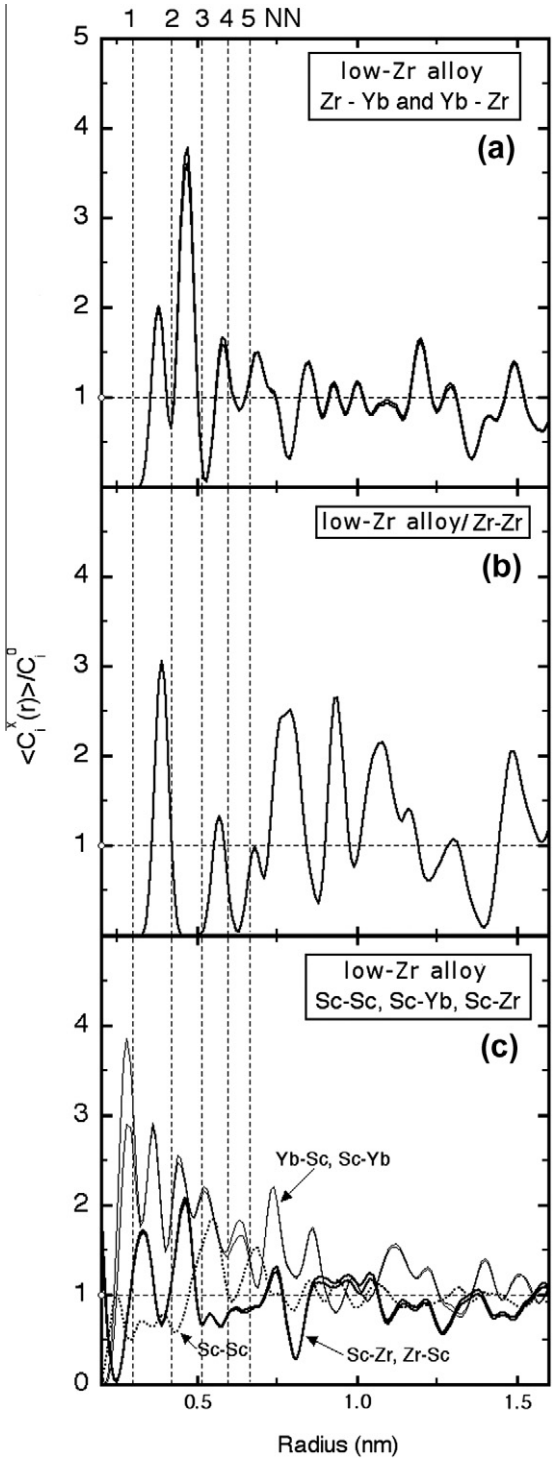

Fig. 9. Partial radial distribution functions (RDFs) for the low Zr alloy in the as-quenched state: (a) Zr–Yb and Yb–Zr; (b) Zr–Zr; (c) all Sc partial RDFs.

$$N(t)_V^{-1} - N(t_o)_{Vo}^{-1} \cong 4.74 \frac{K_{KV}}{\phi^{eq}}(t - t_o) \tag{3}$$

$$\Delta C_i^{\alpha} = \langle C_i^{\alpha,ff}(t)\rangle - C_i^{\alpha,eq}(\infty) = \kappa_{i,KV}^{\alpha} t^{-1/3} \tag{4}$$

where K_{KV} and $\kappa_{i,kV}^{\alpha}$ are the coarsening rate constants for precipitate radius, $\langle R(t)\rangle$, and matrix supersaturation,

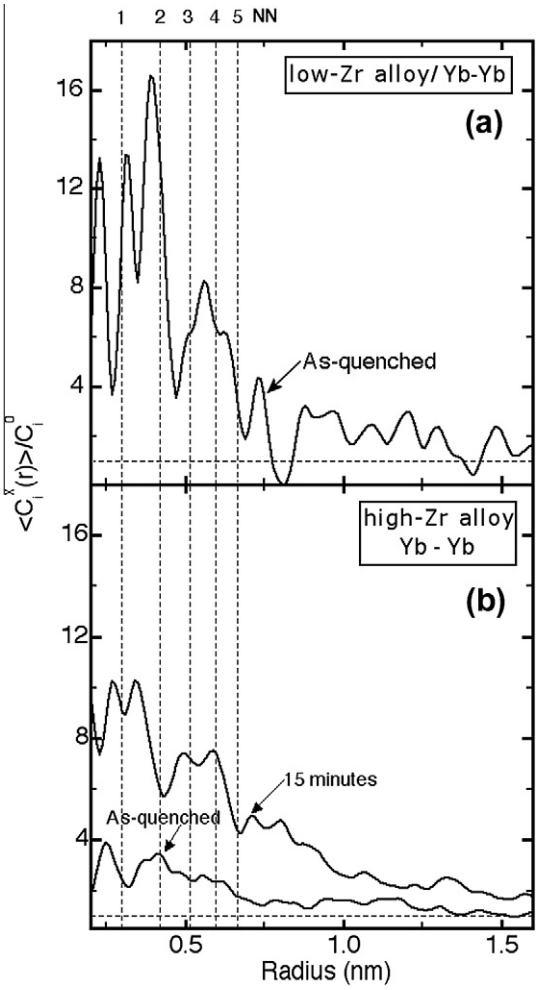

Fig. 10. Partial radial distribution functions (RDFs) for Yb–Yb for the as-quenched state: (a) low Zr; (b) high Zr alloys. (Also including curve for 15 min of aging.)

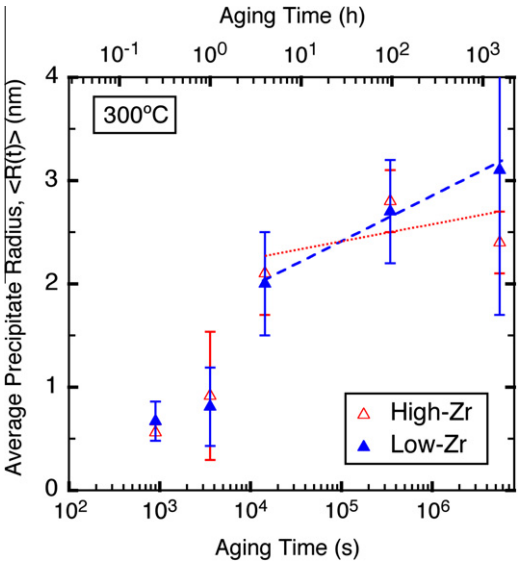

Fig. 11. Average precipitate radius $\langle R\rangle$ versus aging time at 300 °C for low Zr and high Zr alloys. The lines connecting the data points were used to calculate the coarsening rate constants.

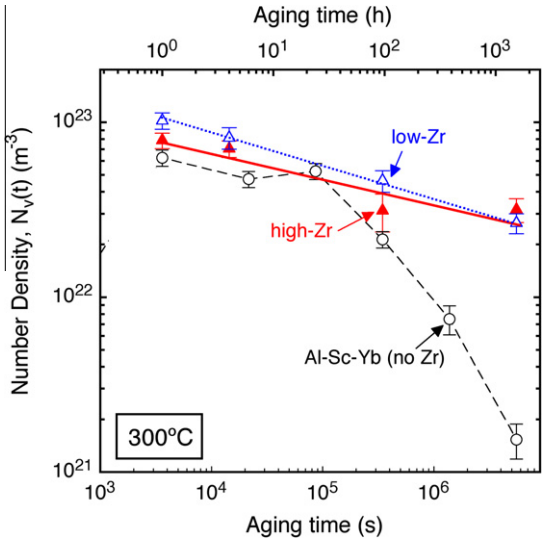

Fig. 12. Number density of precipitates N_v versus aging time at 300 °C for the low Zr and high Zr quaternary alloys, compared with a Zr-free ternary Al–0.06Sc–0.02Yb alloy [34].

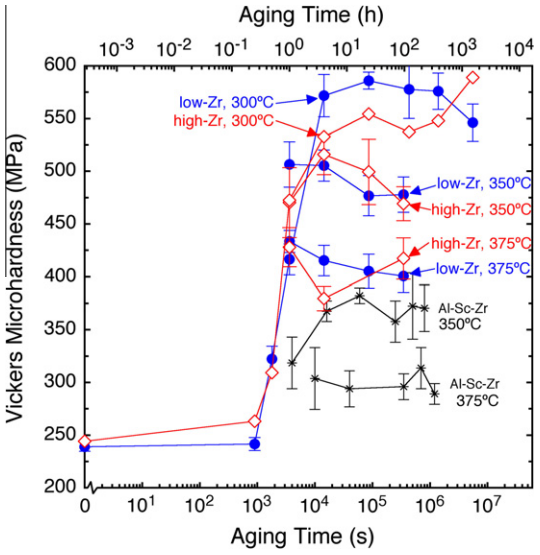

Fig. 13. Vickers microhardness versus aging time at 300, 350 and 375 °C for the low Zr and high Zr alloys. Also plotted for comparison are the aging responses of the Yb-free ternary alloy (Al–0.06Sc–0.005Zr [52]) at 350 and 375 °C.

$\Delta C_i^{\alpha}(t)$, respectively and t_0 is the onset of quasi-stationary coarsening, i.e. the time at which the volume fraction of precipitates φ is asymptotically approaching a constant value ϕ^{eq}. The matrix supersaturation $\Delta C_i^{\alpha}(t)$ is the difference between the concentration in the far field α-Al matrix $\langle C_i^{\alpha,ff}(t)\rangle$ and the equilibrium α-matrix solute solubility $C_i^{\alpha,eq}(\infty)$.

The time exponents for the evolution of $\langle R(t)\rangle$ at 300 °C (Fig. 11) are calculated using a multiple regression analysis (Eq. (2)) to be 0.02 ± 0.04 for the low Zr alloy and 0.07 ± 0.01 for the high Zr alloy, compared with the higher value of 0.18 ± 0.03 for the ternary Al–Sc–Yb alloy [34]. The time exponents are smaller than the 1/3 model value, indicating that coarsening is occurring at a rate slower than the diffusion-limited rate and a quasi-stationary state has not been achieved. These values may, however, not be very useful because as a rule of thumb $\langle R(t)\rangle$ must increase by a factor of 10 to obtain a meaningful value for the exponents. This would, however, require too long a time for practical laboratory studies at 300 °C. For the evolution of N_v at 300 °C the measured time exponent is -0.18 ± 0.01 for the low Zr alloy and -0.17 ± 0.07 for the high Zr alloy (Fig. 12). These values are also smaller than the value of -0.84 ± 0.05 measured previously for the ternary Al–Sc–Yb alloy [34] and are significantly less than the quasi-stationary state coarsening model value of –1.

Due to the excellent microhardness retention by both alloys upon aging at 300 °C (Fig. 1) resulting from the strong coarsening resistance of the precipitates (Figs. 11 and 12), the evolution of microhardness was measured for aging at 350 and 375 °C (Fig. 13). As expected, the peak microhardness values decrease with increasing aging temperature. Once the peak microhardness value is achieved it remains constant up to the longest aging times studied: 96 h at 350 and 375 °C and 1536 h at 300 °C. A similar trend was observed for an Al–0.07Sc–0.02Zr alloy [52], but with smaller peak microhardness values at 350 and 375 °C (Fig. 13). In contrast, for a comparable ternary Al–Sc–Yb alloy without Zr addition the microhardness was noticeably less, 150 MPa, than the peak microhardness after aging for 96 h at 350 °C [34].

3.5. Creep properties at 300 °C

The minimum strain rate $\dot{\varepsilon}$ is plotted as a function of compressive stress σ in Fig. 14 for the two quaternary alloys and the two control ternary Al–Sc–Zr [52] and Al–Sc–Yb [34] alloys with similar $\langle R\rangle$ values (Table 1). All alloys exhibit a large apparent stress exponent, which is

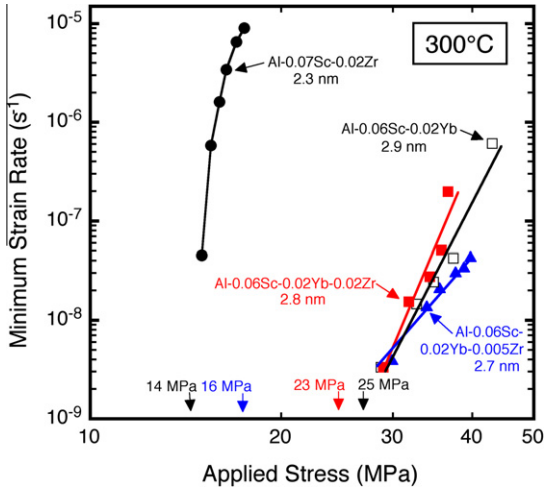

Fig. 14. Double logarithmic plot of minimum strain rate versus applied stress for peak aged alloys subjected to compressive creep at 300 °C. Values of $\langle R\rangle$ are given for each alloy. The calculated threshold stresses are indicated by arrows on the abscissa.

Table 1
Creep threshold stresses at 300 °C and the corresponding average precipitate radii $\langle R(t)\rangle$ for present quaternary Al–Sc–Yb–Zr alloys and control Al–Sc–Zr [52] and Al–Sc–Yb alloys [33].

Alloy (at.%)	Threshold stress (σ_{th}) (MPa)	$\langle R(t)\rangle$ (nm)
Al–0.06Sc–0.02Yb–0.005Zr	16 ± 3	2.7 ± 0.5
Al–0.06Sc–0.02Yb–0.02Zr	23 ± 9	2.8 ± 0.3
Al–0.06Sc–0.02Yb	25 ± 5	2.9 ± 0.5
Al–0.07Sc–0.02Zr	14 ± 1	2.3 ± 0.1

indicative of a threshold stress σ_{th}, determined by plotting $\dot{\varepsilon}^{1/n}$ vs. σ according to:

$$\dot{\varepsilon} = A(\sigma - \sigma_{th})^n \exp\left(-\frac{Q}{R_g T}\right) \quad (5)$$

where A is the Dorn constant, σ is the applied stress, $Q = 142$ kJ mol^{-1} is the activation energy of creep in pure Al [53], $n = 4.4$ is the stress exponent of pure Al [53], and R_g is the ideal gas constant. The threshold stresses of the low and high Zr alloys are 16 ± 3 and 23 ± 9 MPa, with the smaller threshold stress resulting from the smaller slope (Fig. 14). The ternary Al–Sc–Yb and Al–Sc–Zr alloys exhibit threshold stresses of 25 ± 5 and 14 ± 1 MPa, respectively.

4. Discussion

4.1. Precipitate nucleation at 300 °C

4.1.1. Partial radial distribution functions

Zirconium strongly affects the diffusivity of Yb in Al, since the precipitation kinetics in the quaternary Al–Sc–Yb–Zr alloy are slower than in the Zr-free Al–Sc–Yb alloy (Fig. 1). In a recent study on Al–Li–Sc alloys it was shown that the coarsening of $Al_3(Li_{1-x}Sc_x)L1_2$ precipitates occurs at a slower rate than that of $Al_3Li(L1_2)$ in Al–Li [54], which exhibited larger N_v and smaller $\langle R\rangle$ values than in the Sc-free Al–Li alloys. Additionally, Soisson and Martin [55] employed lattice kinetic Monte Carlo (LKMC) simulations to study the effects of small concentrations, as small as 10 at. p.p.m., of generic ternary additions on the formation of clusters. Even at these small concentrations the formation of atomic clusters can either be enhanced or suppressed, depending on the parameters describing the interactions between the dilute alloying elements and vacancies.

It is known that the addition of small concentrations of microalloying elements or impurity atoms can greatly affect the precipitation kinetics of the other solute elements in Al alloys. For example, when 0.1 at.% Si is added to an Al–0.18 at.% Zr alloy there is a 60% increase in the microhardness and a simultaneous decrease in the incubation time for precipitation, since the microhardness is increased in the as-quenched state. This occurs because Si is incorporated into the precipitates on the Al sublattice sites [56]. The addition of 0.1 at.% Si to Al–Hf alloys [57] as well as 0.1 at.% Ag additions to Al–Cu–Mg alloys [58] lead to significant increases in microhardness. In a study on a commercial 6111 aluminum alloy, the increase in strength upon aging at 175 °C for 30 min following pre-aging at 79–107 °C was 60–85 MPa, in contrast to a strength increase of only 20–25 MPa in a sample that had not undergone pre-aging [59]. This is attributed to the clustering of atoms during pre-aging.

There is experimental evidence in different alloy systems for an effect of the diffusivity of one element on another, which gives rise to off-diagonal terms in the diffusion tensor: for example, Fe-, Cu- and Ni-based alloys [60–64]. Diffusivity in the presence of solute atoms has been modeled, with a summary of the different methods given by Nastar [65]. In addition to the overall changes in the diffusive fluxes, the specific atomistic interactions between atoms and their effects on diffusion have been examined. For example, Mao et al. demonstrated that clusters of Al (Al n-mers) and Cr (Cr n-mers) diffuse faster in a Ni matrix, up to pentamers, than an individual Al or Cr atom [64], with Al–Al and Cr–Cr dimers diffusing at the fastest rate. They attributed this behavior to attractive vacancy–solute interactions at distances greater than the first NN distance, specifically, through the fourth NN.

Based on these prior results, the partial RDF results shed light on the interactions among the alloying elements in the Al–Sc–Yb–Zr alloys. The partial Yb–Zr and Zr–Yb RDF (Fig. 8a) demonstrate that attractive interactions exist between the Yb and Zr atoms in the as-quenched state. In the low Zr alloy there is less of an interaction of Yb with Zr atoms (Fig. 9a). This interaction with Zr atoms in the unaged condition, could be one reason why the rate of Yb precipitation decreases on addition of Zr to the Al–Sc–Yb alloy, as Zr has a very small diffusivity in Al [21]. The likelihood that Zr is affecting Yb diffusivity increases if they are in close proximity to one other, i.e. within several NN distances. Beyond ~4 NN distances the data are more difficult to interpret, due to experimental measurement uncertainties as well as decreased distances between NN for larger NN distances. This is not expected to be a serious problem because in metallic alloys the atomic interactions beyond the fourth NN are not anticipated to be strong.

At the 15 min aging time ordered precipitates with the L12 structure are present in the alloy. Since the Sc and Yb atoms are located at the second NN distance in this structure it is expected that the partial RDF of Sc–Sc, Yb–Yb and Sc–Yb display a peak at the second NN distance and a value of less than unity at the first NN distance. This is not observed as the entire curve has values above unity (not just delta functions at the actual positions). This is due to positional errors in the RDF and to peak overlap. Thus only positive correlations can be inferred, rather than specific NN positions.

4.1.2. Zirconium clustering in the precipitates

The partial RDF results indicating that Zr interacts with Yb in the as-quenched state imply that Zr is involved in the

nucleation process. Deschamps et al. [66] suggested that the nucleation of $Al_3Sc(L1_2)$ precipitates is catalyzed by the relatively immobile Zr atoms. Additionally, Fuller and Seidman [12] proposed that $Al_3(Sc_{1-x}Zr_x)(L1_2)$ precipitates in dilute Al–Sc–Zr alloys nucleate on Sc–Sc, Zr–Zr or Sc–Zr dimers or larger clusters. LKMC simulations of Al–Zr–Sc alloys also demonstrate that there is a higher concentration of Zr at the center of the precipitates, which was attributed to Zr being present at the beginning of the precipitation process, a thermodynamic effect [24]. This is unlike the Zr shell engulfing the precipitates, which was attributed to the small diffusivity of Zr in Al, which is a kinetic effect.

Thus if Zr has the same effect on the formation of $Al_3(Sc_{1-x}Yb_x)(L1_2)$ precipitates as in the Al–Zr–Sc alloys it should be present in the precipitates during the nucleation stage. The LEAP tomographic results demonstrate that after 15 min aging very few precipitates contain a Zr atom. In fact, for the high Zr alloy aged for 15 min none of the ~200 clusters and precipitates detected by the envelope method contain a Zr atom. After 1 h aging 8.5% contain a Zr atom. In the low Zr alloy 2.1% of the precipitates contain a Zr atom after 15 min and 0% after 1 h aging. Hence, it is unlikely that the main mechanism of precipitation in these Al–Sc–Yb–Zr alloys involves nucleation on Zr atoms or Zr-containing clusters. Rather, the main effect of Zr seems to be to decrease the diffusivity of Yb. Due to the small diffusivity of Zr in Al the root mean square (RMS) diffusion distance of Zr is insufficient for Zr atoms to reach the precipitates after 1 h. The small Zr concentrations measured in the precipitates even after 1536 h aging, determined using proxigrams, is consistent with this interpretation (Fig. 7).

4.2. Growth and coarsening

4.2.1. Yb/(Yb + Sc) ratio in precipitates created at 300 °C

For both quaternary alloys there is a wide range of precipitate concentrations after 15 min aging (Fig. 4a and b), indicating that the Yb and Sc atoms co-precipitate. Although there is a difference between the average value of $C^{\alpha'}_{Yb}(R)/(C^{\alpha'}_{Yb}(R)+C^{\alpha'}_{Sc}(R))$ in the two Zr-containing alloys, they are more similar to each other than to the Zr-free ternary Al–Sc–Yb alloy, which contains more Yb in smaller precipitates as well as in some larger precipitates (Fig. 4c): $C^{\alpha'}_{Yb}(R)/(C^{\alpha'}_{Yb}(R)+C^{\alpha'}_{Sc}(R))$ is twice as large in the Zr-free ternary Al–Sc–Yb alloy than in the Zr-containing quaternary alloys. The large value of $C^{\alpha'}_{Yb}(R)/(C^{\alpha'}_{Yb}(R)+C^{\alpha'}_{Sc}(R))$ for Al–Sc–Yb is because after 15 min aging over 90% of the Yb atoms had precipitated. Slower precipitation kinetics are observed with Zr-containing alloys: the fraction of the total (Yb + Sc) solute precipitated is smaller by almost one-third for the Zr-containing alloys than for the Zr-free Al–Sc–Yb alloy (Fig. 6).

Simultaneous co-precipitation of Yb and Sc may be one reason for the uniform spatial distribution of Yb and Sc in the precipitates (Fig. 7), the other reason being homogenization within the precipitate. The Yb-rich core/Sc-rich shell structure observed in $Al_3(Sc_{1-x}Yb_x)$ precipitates in ternary Al–Sc–Yb alloys [34,67] is absent in the quaternary alloys. Furthermore, the two stage precipitation process displayed by the Al–Sc–Yb alloy appears to be nonexistent in the Zr-containing quaternary alloys, as there is only one stage of rapid increase in microhardness (Fig. 1). Finally, it is apparent that Zr segregates at the matrix/precipitate interface at longer aging times (Fig. 7), in agreement with the APT observations for Al–Sc–Zr alloys [23] discussed above, which is a kinetic effect due to the small diffusivity of Zr in Al. The Zr interfacial excess at the matrix/precipitate interface may, however, be a result of local thermodynamic equilibrium.

4.2.2. Precipitate size distributions and nucleation currents upon aging at 300 °C

After 1 h aging the precipitate size distribution (PSD) is bi-modal in the high Zr alloy (Fig. 3c): sub-critical precipitates (i.e. embryos) exist below a critical radius, R^*, while for $R > R^*$ precipitates are present. R^* lies at the trough between the two peaks of PSD, and its value is estimated from Fig. 3c to be $R^* \approx 1$ nm, which is similar to the value found in Ni–Al alloys by Xiao and Haasen [68]. For the low Zr alloy a bi-modal PSD of precipitates is not evident (Fig. 3d), since there are only a few precipitates with $R > 1$ nm. The quantity N_v (Fig. 12) is calculated using $R^* = 1$ nm for both alloys, resulting in similar values of N_v for the two Zr-containing alloys, as well as the Al–Sc–Yb alloy.

After a shorter 15 min aging time there are only precipitates with $R < 1$ nm in the high Zr alloy (Fig. 3a), while the low Zr alloy shows only a few precipitates with $R > 1$ nm (Fig. 3b). Since there are only small precipitates, a bi-modal distribution is not observed, and an R^* value cannot be estimated for the 15 min aging time.

The nucleation currents, estimated from the increase in N_v values from the unaged condition through the 1 h aging time, were $2.8 \times 10^{19}\ m^{-3}\ s^{-1}$ and $2.4 \times 10^{19}\ m^{-3}\ s^{-1}$ for the low and high Zr alloys, respectively. These are smaller than the value of $1.9 \times 10^{20}\ m^{-3}\ s^{-1}$ measured for the Zr-free Al–Sc–Yb alloy [34]. The nucleation currents for the quaternary Al–Sc–Yb–Zr alloys are, however, greater than those measured employing transmission electron microscopy in an Al–0.11 at.% Sc alloy [2], for which values of 9×10^{18} and $1.01 \times 10^{19}\ m^{-3}\ s^{-1}$ were measured at 288 and 343 °C. This implies that a very small solute concentration of Zr has a strong effect on the nucleation current.

4.2.3. Coarsening model applicability

The time exponents for $\langle R(t)\rangle$ are smaller than the 1/3 model value, indicating that coarsening is occurring at a rate slower than the diffusion-limited rate and a quasi-stationary state has not been achieved, as assumed in the model. These values may, however, not be very useful since a practical rule of thumb states that $\langle R(t)\rangle$ must increase by a factor of 10 to obtain a meaningful value of the exponent. This would, however, require too long a time for practical

laboratory studies at 300 °C. Additionally, this model was developed for a ternary model and herein we are examining a quaternary alloy, whose precipitation is quite complex. Thirdly, while our alloys are quite dilute, they are not ideal solid solutions.

4.2.4. Aging at 350 and 375 °C

In Section 3.4 we reported that quaternary Al–Sc–Yb–Zr alloys have slow coarsening kinetics at 300 °C with temporal exponents and coarsening constants smaller than Zr-free Al–Sc–Yb alloys. Furthermore, at higher temperatures the quaternary alloys exhibit fairly constant values of Vickers microhardness upon aging at 350 or 375 °C (Fig. 13), indicating that once the precipitates form they grow and coarsen slowly. Both the low and high Zr alloys have similar microhardness values for the same aging treatment, confirming that only a small concentration of Zr (<50 at. p.p.m.) is sufficient to markedly improve the coarsening resistance of Al_3Sc precipitates.

Similar to the Al–Sc–Zr alloys [52] (C.B. Fuller, personal communication, 2002), the Al–Sc–Yb–Zr alloys retain their peak microhardness values for aging times of several hundred hours. Similar additions of 200 at. p.p.m. Zr to Al–0.07 Sc significantly improved the coarsening resistance [12]. The quaternary alloys have somewhat larger microhardness values at a given temperature than the Al–Sc–Zr alloy, for example 375 versus 500 MPa peak microhardness at 350 °C, which could be the result of differences in the precipitation kinetics. Finally, the Al–Sc–Yb–Zr alloys maintain their microhardness up to 96 h aging, whereas, the Zr-free Al–Sc–Yb alloy displayed a microhardness decrease of 100 MPa between 24 and 96 h aging at 350 °C, which is a result of a higher coarsening rate of the precipitates [33].

4.3. Creep properties at 300 °C

Fig. 14 shows that the three Yb-containing alloys (the prior ternary Al–Sc–Yb alloy [34] and the present two quaternary Al–Sc–Yb–Zr alloys) have much higher creep resistances (i.e. the values of the threshold and flow stresses for a given strain rate) at 300 °C than the Yb-free ternary Al–Sc–Zr alloy [52], despite very similar solute concentrations and precipitate sizes (Table 1). This confirms prior research showing that a RE element such as Yb [35,67], which increases the lattice parameter mismatch between the precipitates and the matrix, improves creep resistance because of an increase in elastic interactions between precipitates and dislocations [32]. The present creep results for the low Zr and high Zr alloys are consistent with this model. The lattice parameter mismatch for an $Al_3(Sc_{0.75}Yb_{0.25})$ precipitate with an α-Al matrix is 1.65% at 300 °C [27,69], assuming a uniform distribution of Yb and Sc atoms in the precipitate phase. The lattice parameter mismatch in the ternary alloy is significantly greater than the value of 1.048% for Al_3Sc in binary Al–Sc at 300 °C [69]. In contrast, the addition of Zr to Al_3Sc precipitates has a negligible effect on the lattice parameter mismatch with Al: for $Al_3(Sc_{0.75}Zr_{0.25})$ it is 1.047%. Hence, it is likely that the Al_3(Sc,Yb,Zr) precipitates in the quaternary alloys have lattice parameter mismatches similar to those of Al_3(Sc,Yb) precipitates in the ternary Al–Sc–Yb alloy [34], explaining their similar creep resistance behavior. The enrichment of Zr in a shell enveloping the precipitate cores is unlikely to significantly change the long-range strain field of the precipitates, which through its interactions with dislocations dictates the threshold stress [32].

5. Conclusions

The effects of Zr and Yb additions to dilute Al–Sc alloys on their microstructural evolution at 300–375 °C and creep properties at 300 °C were studied. Comparing two quaternary alloys (Al–0.06Sc–0.02Yb–0.02Zr and Al–0.06Sc–0.02Yb–0.005Zr (at.%)) with two ternary alloys (Al–0.06Sc–0.02Yb and Al–0.07Sc–0.02Zr), it was demonstrated that Zr and Yb have the following effects.

- Zr decreases the precipitation kinetics in the quaternary Al–Sc–Yb–Zr alloys, as evidenced by an approximately one-third reduction in the amount of solute precipitated after aging for 1 h at 300 °C, compared with a Zr-free Al–Sc–Yb alloy.
- The quaternary Al–Sc–Yb–Zr alloys show a single rapid increase in microhardness after an initial incubation period of 5–15 min aging at 300 °C, indicative of simultaneous precipitation of Sc and Yb in Al_3(Sc,Yb,Zr) precipitates. This is in contrast to a ternary Zr-free Al–Sc–Yb alloy [34], which exhibits a distinct two stage precipitation sequence, where Yb-rich Al_3(Yb, Sc) precipitates are initially formed with an increase in Sc concentration during subsequent growth and coarsening. Thus it appears that Zr affects the diffusivity of Yb in the matrix during precipitation, which is confirmed by partial RDF results indicating an attractive interaction between Zr and Yb atoms in the quaternary alloys.
- Atom probe tomographic studies confirm that Yb and Sc solute atoms precipitate simultaneously from solid solution. After 15 min aging at 300 °C the Yb concentration in the precipitates is about three times greater than expected based on the average alloy composition, indicating faster precipitation kinetics for Yb compared with Sc. These results also demonstrate that the majority of precipitates do not nucleate on Zr atoms, as there are no detectable Zr atoms in >90% of the precipitates formed at 300 °C. Only at longer aging times at 300 °C does Zr precipitate, forming a Zr-enriched shell enveloping the Al_3(Sc,Yb,Zr) precipitates. These precipitates are very coarsening resistant up to 375 °C.
- The peak aged quaternary Al–Sc–Yb–Zr alloys show creep resistance at 300 °C similar to Zr-free ternary Al–Sc–Yb alloys, but much improved with respect to the Yb-free Al–Sc–Zr alloy. This confirms the strong

effect on creep resistance of lattice parameter mismatch between the precipitates and α-Al matrix, which is increased by the presence of Yb but unaffected by Zr.
- In summary, the quaternary Al–Sc–Yb–Zr alloys have the combined advantages of good creep resistance, as observed in ternary Al–Sc–Yb, and high coarsening resistance, as in Al–Sc–Zr.

Acknowledgements

This research was supported through Grant DE-FG02-98ER45721 from the US Department of Energy (Basic Energy Sciences, monitor Dr. John Vetrano). Atom probe tomographic measurements were performed at the Northwestern University Center for Atom-Probe Tomography (NUCAPT) using a LEAP tomograph purchased with funding from the NSF-MRI (DMR-0420532, monitor Dr. Charles Bouldin) and ONR-DURIP (N00014-0400798, monitor Dr. Julie Christodoulou) programs.

References

[1] Knipling KE, Dunand DC, Seidman DN. Z Metallkd 2006;97:246.
[2] Hyland RW. Metall Trans A 1992;23A:1947.
[3] Jo HH, Fujikawa SI. Mater Sci Eng A 1993;171:151.
[4] Nakayama M, Furuta A, Miura Y. Mater Trans JIM 1997;38:852.
[5] Novotny GM, Ardell AJ. Mater Sci Eng A 2001;A318:144.
[6] Marquis EA, Seidman DN. Acta Mater 2001;49:1909.
[7] Iwamura S, Miura Y. Acta Mater 2004;52:591.
[8] Royset J, Ryum N. Mater Sci Eng A 2005;396:409.
[9] Fuller CB, Seidman DN, Dunand DC. Scripta Mater 1999;40:691.
[10] Marquis EA, Seidman DN, Dunand DC. Acta Mater 2002;50:4021.
[11] Van Dalen ME, Dunand DC, Seidman DN. Acta Mater 2005;53:4225.
[12] Fuller CB, Seidman DN. Acta Mater 2005;53:5415.
[13] Hallem H, Lefebvre W, Forbord B, Danoix F, Merthinsen K. Mater Sci Eng A 2006;421:154.
[14] Fuller CB. PhD thesis. Northwestern University, Evanston, IL; 2003. <http://arc.nucapt.northwestern.edu/refbase/show.php?record=147>.
[15] Lefebvre W, Danoix F, Hallem H, Forbord B, Bostel A, Marthinsen K. J Alloys Compd 2009;470:107.
[16] Toropova LS, Eskin DG, Kharakterova ML, Dobatkina TV. Advanced aluminum alloys containing scandium. Amsterdam: Gordon & Breach; 1998.
[17] Harada Y, Dunand DC. Mater Sci Eng A 2002;329–331:686.
[18] Forbord B, Lefebvre W, Danoix F, Hallem H, Marthinsen K. Scripta Mater 2004;51:333.
[19] Knipling KE, Karnesky RA, Dunand DC, Seidman DN. Acta Mater 2010;58:5184.
[20] Knipling K, Seidman DN, Dunand DC. Acta Mater 2011;59:943.
[21] Fujikawa SI. Defect Diffus Forum 1997;143–147:115.
[22] Tolley A, Radmilovic V, Dahmen U. Scripta Mater 2005;52:621.
[23] Fuller CB, Murray JL, Seidman DN. Acta Mater 2005;53:5401.
[24] Clouet E, Lae L, Epicier T, Lefebvre W, Nastar M, Deschamps A. Nat Mater 2006;5:482.
[25] Clouet E, Nastar M, Barbu A, Sigli C, Martin G. Solid–solid phase transformations in inorganic materials. Warrendale (PA): TMS; 2005. p. 1.
[26] Zalutskaya OI, Kontseyoy VG, Karamishev NI, Ryabov VR, Zalutskii II. Dopovidi Akademii Nauk Ukr RSR; 1970. p. 751.
[27] Palenzona AJ. J Less-Common Metals 1972;29:289.
[28] Harada Y, Dunand DC. Intermetallics 2009;17:17.
[29] Van Dalen ME, Karnesky RA, Cabotaje JR, Dunand DC, Seidman DN. Acta Mater 2009;57:4081.
[30] Mondolfo LF. Aluminum alloys: structure and properties. London: Butterworths; 1976.
[31] Bergner D, Chi NV. Wissenschaftliche Zeitschrift der Padagogischen Hochschule "N.K. Krupskaja". Halle XV, Heft 3; 1977.
[32] Marquis EA, Dunand DC. Scripta Mater 2002;47:503.
[33] van Dalen ME. PhD thesis, Northwestern University, Evanston, IL, 2007. <http://arc.nucapt.northwestern.edu/refbase/show.php?record=9848>.
[34] van Dalen ME, Dunand DC, Seidman DN. Acta Mater 2011;59:5224.
[35] Karnesky RA, Seidman DN, Dunand DC. Mater Sci Forum 2006;519–521:1035.
[36] Karnesky RA, Van Dalen ME, Dunand DC, Seidman DN. Scripta Mater 2006;55:437.
[37] Krug ME, Werber A, Dunand DC, Seidman DN. Acta Mater 2010;58:134.
[38] Kelly TF, Gribb TT, Olson JD, Martens RL, Shepard JD, Wiener SA, et al. Microsc Microanal 2004;10:373.
[39] Hellman OC, Vandenbroucke JA, Rüsing J, Isheim D, Seidman DN. Microsc Microanal 2000;6:437.
[40] Hellman OC, Vandenbroucke J, Blatz du Rivage J, Seidman DN. Mater Sci Eng A 2002;327:29.
[41] Miller MK. Atom probe tomography: analysis at the atomic level. New York: Kluwer Academic; 2000.
[42] Hyde JM, English CA. Proc of MRS Fall 2000 Meeting, vol. 650; 2001. p. 1.
[43] Knipling K, Dunand DC, Seidman DN. Microsc Microanal 2007;13:503.
[44] Goodman SR, Brenner SS, Low Jr JR. Metall Trans 1973;4:2363.
[45] Goodman SR, Brenner SS, Low Jr JR. Metall Trans 1973;4:2371.
[46] Sudbrack CK, Noebe RD, Seidman DN. Phys Rev B 2006;73:212101.
[47] De Geuser F, Lefebvre W, Blavette D. Philos Mag Lett 2006;86:227.
[48] Ziman JM. Models of disorder: the theoretical physics of homogeneously disordered systems. Cambridge: Cambridge University Press; 1979.
[49] Vurpillot F, Bostel A, Blavette D. Appl Phys Lett 2000;76:3127.
[50] Vurpillot F, Cerezo A, Blavette D, Larson D. Microsc Microanal 2004;10:384.
[51] Kuehmann CJ, Voorhees PW. Metall Mater Trans A 1996;27A:937.
[52] Fuller CB, Seidman DN, Dunand DC. Acta Mater 2003;51:4803.
[53] Frost HJ, Ashby MF. Deformation-mechanism maps: the plasticity and creep of metals and ceramics. Oxford (UK): Pergamon; 1982.
[54] Joh CH, Yamada K, Miura Y. Mater Trans JIM 1999;40:439.
[55] Soisson F, Martin G. Phys Rev B 2000;62:203.
[56] Sato T, Kamio A, Lorimer G. Mater Sci Forum 1996;217–222:895.
[57] Hallem H, Forbord B, Marthinsen K. Mater Sci Eng A 2004;387:940.
[58] Ringer SP, Sakurai T, Polmear IJ. Acta Mater 1997;45:3731.
[59] Bryant JD. Metall Mater Trans A 1999;30A:1999.
[60] Kirkaldy JS, Young DJ. Diffusion in the condensed state. London: The Institute of Metals; 1987.
[61] Barros J, Malengier B, Van Keer R, Houbaert Y. J Phase Equilib Diffus 2005;26:417.
[62] Divinski SV, Hisker F, Herzig C, Filipek R, Danielewski M. Defect Diffus Forum 2005;237–240:50.
[63] Hayashi S, Wang W, Sordelet J, Gleeson B. Metall Mater Trans A 2005;36A:1769.
[64] Mao Z, Sudbrack CK, Yoon KE, Martin G, Seidman DN. Nat Mater 2007;6:210.
[65] Nastar M. Philos Mag 2005;85:3767.
[66] Deschamps A, Lae L, Guyot P. Acta Mater 2007;55:2775.
[67] Van Dalen ME, Dunand DC, Seidman DN. J Mater Sci 2006;41:7814.
[68] Xiao SQ, Haasen P. Acta Metall Mater 1991;39:651.
[69] Harada Y, Dunand DC. Scripta Mater 2003;48:219.